Evidence for chiral graviton modes in fractional quantum Hall liquids

Jiehui Liang[1*], Ziyu Liu[2*], Zihao Yang[1], Yuelei Huang[1], Ursula Wurstbauer[3], Cory R. Dean[2], Ken W. West[4], Loren N. Pfeiffer[4], Lingjie Du[1,5ǂ], Aron Pinczuk[2,6]

[1] School of Physics, National Laboratory of Solid State Microstructures, and Collaborative Innovation Center for Advanced Microstructures, Nanjing University, Nanjing 210093, China

[2] Department of Physics, Columbia University, New York, New York 10027, USA

[3] Institute of Physics, University of Münster, Wilhelm-Klemm-Str.10, 48149 Münster, Germany

[4] Department of Electrical Engineering, Princeton University, Princeton, New Jersey 08544, USA

[5]Shishan Laboratory, Suzhou Campus of Nanjing University, Suzhou 215000, China

[6] Department of Applied Physics and Applied Mathematics, Columbia University, New York, New York 10027, USA

**These authors contribute equally to this work*

ǂCorresponding author. Email: ljdu@nju.edu.cn

Exotic physics could emerge from interplay between geometry and correlation. In fractional quantum Hall (FQH) states[1], novel collective excitations called chiral graviton modes (CGMs) are proposed as quanta of fluctuations of an internal quantum metric under a quantum geometry description[2-5]. Such modes are condensed-matter analogues of gravitons that are hypothetical spin-2 bosons. They are characterized by polarized states with chirality[6-8] of +2 or -2, and energy gaps coinciding with the fundamental neutral collective excitations (i.e., magnetorotons[9,10]) in the long-wavelength limit. However, CGMs remain experimentally inaccessible. Here, we observe chiral spin-2 long-wavelength magnetorotons using inelastic scattering of circularly-polarized lights, providing strong evidence for CGMs in FQH liquids. At filling factor ν = 1/3, a gapped mode identified as the long-wavelength magnetoroton emerges under a specific polarization scheme corresponding to angular momentum S = -2, which persists at extremely-long wavelength. Remarkably, the mode chirality remains -2 at ν = 2/5 but becomes the opposite at ν = 2/3 and 3/5. The modes have characteristic energies and sharp peaks with marked temperature and filling-factor dependence, corroborating the assignment of long-wavelength magnetorotons. The observations capture the essentials of CGMs and support the FQH geometrical description, paving the way to unveil rich physics of quantum metric effects in topological correlated systems.

Main

Substantial advancements in geometrical interpretations of condensed matter systems have propelled quantum metric effects to the forefront of intense research[2-8,11-25]. Examples include the anomalous and nonlinear Hall effects[23-25] as well as collective excitations of FQH states[2-10,18-20]. The FQH effect[1] presents a paradigm of topological order arising in two-dimensional electron gases (2DEGs) under strong perpendicular magnetic fields $B_\perp$. Collective excitations play a key role in the FQH effect, with their dispersion governing the rich correlation physics. In the FQH states at $\nu = p/(2p+1)$ (p = integer), correlation gives rise to incompressible liquids and is often described in terms of composite fermions (CFs) where each electron is bound by two flux quanta. CFs move in circular orbits (Fig. 1a) with Landau-like energy levels, responsible for fruitful topological phenomena, and excitations between adjacent orbits (or CF Landau levels) determine magnetoroton gaps[26]. Recently, Haldane introduced the concept of quantum geometry[2] to the FQH effect, suggesting the existence of an intrinsic quantum dynamic metric as a new geometrical degree of freedom emerging from correlation. Phenomenologically, the quantum metric specifies the shape of CF orbits (or shape of fundamental droplets[15]) which characterizes the FQH states and can be tuned. Fluctuations of the metric distort the orbits (Fig. 1a) and give rise to spin-2 collective excitations as graviton modes[3,5]. In the FQH states, only chiral modes (CGMs) are allowed[6-8], which carry $S = -2$ for electron states or +2 for their particle-hole conjugates (Fig. 1b) and possess certain gap energies.

CGMs have been studied the most in the $\nu = 1/3$ Laughlin state, with similar physics applicable to the Jain states[8,19,20]. At $\nu = 1/3$, the magnetoroton, proposed by Girvin, MacDonald and Platzman in the single-mode approximation[9], has an energy minimum[27,28] $\Delta_{\mathrm{m}}^{\mathrm{R}}$ analogous to the roton in helium, and can be described by one quasiparticle-quasihole pair of CFs[29] separated by a distance proportional to wavevector q (Fig. 1c). In the long-wavelength limit ($q \approx 0$), the excited CF overlaps its quasihole; then, the magnetoroton has dipole spectral weight vanishing quickly with $(ql_{\mathrm{B}})^4$ ($l_{\mathrm{B}} = \sqrt{\hbar c/eB_\perp}$ is the magnetic length), and was considered optically invisible[9,10,30]. Nevertheless, according to the FQH geometrical description[3,5,6,17], as the distance approaches zero at $q \approx 0$, metric fluctuations of the ground state would become the most effective and develop a quadrupole moment with the spin-2 CGM triggered between adjacent CF LLs (Fig. 1c). As a result, CGMs possess the gap energies of the long-wavelength magnetorotons[9,10] Δ_{m}^{0}, which equivalently are chiral spin-2 long-wavelength magnetorotons[3,6] (CS2LMs). Interestingly, while the Fierz-Pauli field equations[31] in 3+1-dimensions (3+1D) were proposed to describe massive spin-2 bosons (i.e., massive gravitons), the equations for CS2LMs were found[32,33] from the 2+1D Fierz-Pauli field equations in the nonrelativistic limit, thereby revealing the quasiparticle nature of CGMs. Owing to their spin-2 components[5-7], CGMs would have quadrupole spectral weight dominant in Δ_{m}^{0}, which are sensitive to two-photon processes like in resonant inelastic light scattering (RILS).

In experiments, the search for CS2LMs remains an open question. RILS offers direct access to low-lying collective excitations in the FQH regime[10,27,28,34-37], providing critical examinations on the modelling of the FQH liquids[9,29]. In conventional unpolarized RILS studies, energy gaps of long-wavelength magnetorotons were investigated at $\nu = 1/3$ (refs. 10,27) and other FQH states[28,34], manifesting incompressibility of the correlated liquids at macroscopic length scales. However, angular momenta of these modes have not been accessed since incident and scattered lights in the unpolarized setup possess linearly-polarized photons. Circularly-polarized RILS (CP-RILS) experiments that switch circular polarizations of incident and scattered photons could simultaneously probe their excitation gaps and angular momenta[6,7], which are highly desirable to reveal CGMs in the FQH effect.

Here, we report CP-RILS measurements that provide direct observation of chiral spin-2 long-wavelength magnetorotons at $\nu = 1/3$ and its resembling fractional fillings. We locate collective modes at Δ_m^0 in RILS spectra by their energies in magnetoroton dispersions. Remarkably, the modes are observed to possess polarization states of angular momentum S = -2 for ν = 1/3 and 2/5 or S = +2 for ν = 2/3 and 3/5. Furthermore, sharp peaks of the spin-2 modes suggest that the modes have long wavelength; the mode energies at $\nu = p/(2p+1)$ excellently follow the energy scaling $\Delta_m^0 \propto E_c/|2p+1|$ ($E_c=e^2/\varepsilon l_B$ is the Coulomb energy, ε is the dielectric constant), confirming the magnetoroton characteristics of these long-wavelength modes. These modes are found sensitive to elevated temperatures and deviated filling factors away from the incompressible FQH states, behaviors indicative of magnetorotons. Our findings thus provide the first experimental evidence that FQH liquids harbor exotic quasiparticles of CGMs, and reveal the emergence of the quantum metric in topological orders.

Excitations in RILS at ν = 1/3

An ultra-high-mobility 2DEG in a GaAs quantum well (QW) is measured in a backscattering configuration at an angle of incidence θ shown in Fig. 1d (see Methods). This configuration transfers wavevector k of photons to FQH liquids and excites long-wavelength excitations (e.g., $q = k \approx 0.05/l_B$ at $\theta = 25°$). Nevertheless, weak residual disorder could break wavevector conservation[27,28], thus allowing to detect modes with $ql_B \gtrsim 1$. Low-lying excitations in FQH liquids are rare and can be probed using well-established methods in RILS studies[10,27,28,34]. Figure 1e presents RILS spectra of collective excitations at ν = 1/3 in the unpolarized geometry with $\theta = 25°$. Spin-wave excitations at $q \ll 1/l_B$ (Δ_s^0) and at large-q (Δ_s^∞) are located in Fig. 1e (see Methods). Dramatic dependence on temperature and filling factor distinguishes three collective magnetoroton modes[10,27] at ν = 1/3 (see Extended Data Fig. 1). We compare these modes with the calculated dispersion scaled down from the ideal 2D result[29] (the dashed red line in Fig. 1f), facilitating the specific assignments of Δ_m^0, Δ_m^R, and the mode Δ_m^∞ with peaked density of states at large q (see Methods).

CP-RILS at ν = 1/3

The chirality characteristic of Δ_m^0 could be resolved by CP-RILS[5-7] (see Methods). Figure 2a sketches all circularly-polarized (CP) scattering geometries (RR, LL, RL and LR) employed in CP-RILS with right- (R) or left- (L) CP incident and scattered photons. According to angular momentum conservation, the angular momentum transferred to FQH liquids equals the change in the photon spin during light scattering. For example, a mode with S = -2 would be excited when the incident photon has spin -1 and the scattered one has spin +1; this process corresponds to both incident and scattered lights that are right-circularly polarized (RR). A mode with a well-defined chirality should dominate in one specific CP geometry corresponding to a certain angular momentum[5-7]; otherwise, the mode would be active in different CP geometries.

The unpolarized RILS spectrum of Δ_m^0 (Fig. 2b) can be considered as mixed signals from various CP geometries. As shown in Fig. 2c, CP-RILS resolves different CP components of the unpolarized signals. It can be readily found that Δ_m^0 only appears in the RR geometry where two photons transfer spin angular momentum -2 into the FQH state. The mode has marked intensity dependence on incident photon energies ω_L, which is peculiar to RILS (Fig. 2d). In other CP geometries, the mode is suppressed with photoluminescence (PL) background dominating the spectral line-shape (e.g., LR in Supplementary Fig. 1). In sharp contrast to Δ_m^0, Δ_m^R that is well-defined in the magnetoroton dispersion displays finite intensity in all CP geometries (Fig. 2e). The simultaneous occurrence of this mode with both $|S| = 0$ and $|S| = 2$ indicates that it does not carry a certain chirality. The results thus reveal that Δ_{m}^{0} at $\nu = 1/3$ has a specific chirality with $S = -2$.

Figure 2f demonstrates that the spin-2 mode has a quite sharp profile (with PL background subtracted as shown in Extended Data Fig. 2), characterized by full width at half maximum (FWHM) of 30 μeV. Its FWHM that is close to the one of Δ_{s}^{0} at $q = k \ll 1/l_{\mathrm{B}}$, suggests that the spin-2 mode has its wavevector conserved in the scattering[10] and is at long wavelength (see Methods), consistent with our assignment of this mode in Fig. 1e. In contrast, $\Delta_{\mathrm{m}}^{\infty}$ and $\Delta_{\mathrm{s}}^{\infty}$ have larger widths due to weak residual disorder[27,28]. As temperature increases, the spin-2 mode quickly collapses below 800 mK (Fig. 2g). We also find that this mode rapidly quenches when the filling factor is away from $\nu = 1/3$ (Supplementary Fig. 2). The striking temperature and filling-factor dependent behaviors, fingerprints of the FQH effect, suggest that the spin-2 mode highly relies on the incompressibility and correlation of the $\nu = 1/3$ state.

CP-RILS at an extremely small wavevector

In RILS, the wavevector transferred to the 2DEG can be tuned by varying θ. By decreasing θ to 10°, we are able to probe modes at an extremely small $kl_{\mathrm{B}} \approx 0.02$. This value is significantly lower than typical ones ($kl_{\mathrm{B}} \gtrsim 0.05$) reported in previous studies[28,34], allowing us to approach the $q = 0$ limit. In the following, all experiments are performed at $\theta = 10°$ unless noted otherwise. Similar with the result in Fig. 1e, the unpolarized RILS spectra at $\nu = 1/3$ identify Δ_{m}^{0} at 0.66 meV (Extended Data Fig. 3). Then we perform CP-RILS measurements to resolve CP components of this mode. Figure 3a shows a single peak in the RR geometry (corresponding to $S = -2$) coinciding with Δ_{m}^{0} (Extended Data Fig. 4a) and no such peak is found in other geometries (corresponding to $S = +2$ and 0, such as LR in Extended Data Fig. 4b), reproducing the observation at $kl_{\mathrm{B}} \approx 0.05$. We also examine angular momentum of Δ_{m}^{0} by reversing the magnetic field direction and find that it remains -2. These results demonstrate that angular momenta of Δ_{m}^{0} keep constant and are equal to -2 at long wavelength, confirming long-wavelength magnetorotons as chiral spin-2 modes at $\nu = 1/3$.

The CP-RILS spectra show that the energy ratio of the spin-2 mode to $\Delta_{\mathrm{m}}^{\mathrm{R}}$ reaches 2.07 at $kl_{\mathrm{B}} \approx 0.02$ and decreases by 15% at $kl_{\mathrm{B}} \approx 0.05$ (Extended Data Fig. 5). The results agree well with the expected values[9,29] for Δ_{m}^{0} (ratios at $k \approx 0$ are in a range from 2.02 to 2.27 and diminish at larger k) and exclude the alternative explanation of two-roton bound states (see Methods). Moreover, as kl_{B} is reduced by a factor of 2.5, the measured intensities of Δ_{m}^{0} remain comparable (Figs. 2c and 3a), which is hard to be explained by the dipole picture for Δ_{m}^{0} (see Methods). According to the graviton picture[5,7], the mode intensity is determined by the spectral densities of the spin-2 components of the kinetic stress tensor and remains finite even in the long-wavelength limit, which could account for our experimental observations.

Chiralities of the spin-2 modes

The chirality of Δ_{m}^{0} is further examined in the $\nu = 2/3$ state, the particle–hole symmetric counterpart of the $\nu = 1/3$ state. Employing the same methodology as described above, the magnetoroton modes are identified in the unpolarized RILS measurements (Supplementary Fig. 3).

Remarkably, the CP-RILS spectra of Δ_{m}^{0} (Fig. 3b) demonstrate one peak only in the LL geometry corresponding to S = +2 and PL backgrounds dominate the spectra in other CP geometries with no RILS peaks found (such as LR in Supplementary Fig. 4), suggesting that Δ_{m}^{0} has angular momentum +2 at ν = 2/3. Mention that if a mode exists, typically the overlapping strong PL background would resonantly enhance the RILS peak, as seen for Δ_{m}^{0} in RR at ν = 1/3 (see Methods); otherwise, despite the strong PL background, no RILS peak would appear, e.g., in LR at ν = 1/3 (Figs. 2c and 3a). On the other hand, in the absence of prominent PL, a collective mode if existing should still lead to RILS peaks, albeit weak, such as Δ_{m}^{0} in LL at ν = 2/3. Notably, at ν = 2/3, the energy of the spin-2 mode has the same value as that at ν = 1/3 in the unit of E_{c} (0.048 E_{c}), manifesting the same nature of the modes as long-wavelength magnetorotons.

The physics of the chiral spin-2 modes at ν = 1/3 and 2/3 is applicable to the ν = 2/5 and 3/5 Jain states[8,19]. At ν = 2/5, magnetoroton modes can be viewed as excitations of CFs from the second filled CF Landau level to the next unoccupied one. Following the approach in Ref. 28, at ν = 2/5 we perform unpolarized RILS measurements that locate Δ_{m}^{0} at 0.39 meV (Supplementary Fig. 5). Figure 3c shows that Δ_{m}^{0} in CP-RILS spectra has the circular polarization dependence in resemblance to that at ν = 1/3, i.e., the spectra exhibit a well-defined Δ_{m}^{0} peak in the RR geometry (S = -2) with no peaks appearing in other CP geometries. Correspondingly, at ν = 3/5, the circular polarization dependence of Δ_{m}^{0} coincides with that at ν = 2/3 and clearly exhibits a sharp peak only in the LL geometry with S = +2 (Fig. 3d). Moreover, the Δ_{m}^{0} energy at ν = 3/5 has the same value in the unit of E_{c} as that at ν = 2/5, originating from the particle-hole symmetry. As summarized in Fig. 4a, our results clearly demonstrate that long-wavelength magnetorotons have polarization states with chirality of -2 (+2) in the ν = 1/3 and 2/5 (ν = 2/3 and 3/5) states, i.e., being chiral spin-2 modes.

Long-wavelength magnetoroton nature

Figure 4b displays the FWHM of these spin-2 modes, which are around 30 μeV (see details of PL background subtraction from CP-RILS spectra in Extended Data Fig. 6). Such sharp peaks confirm the long-wavelength essence of these modes as discussed in Fig. 2f. In FQH states, magnetoroton gap energies are determined by CFs moving in their orbits under effective magnetic fields $B^*=B_{\perp}-B_{1/2}$ ($B_{1/2}$ is the perpendicular magnetic field at ν = 1/2), which are proportional[34,38,39] to $E_{\mathrm{c}}/|2p+1|$ (also see Extended Data Fig. 7). In our experiments, the spin-2 modes are gapped in the FQH states with extracted energies shown in Fig. 4c, and disappear quickly at deviated filling factors (see Figs. 4d and 4e, Extended Data Fig. 8). Remarkably, as illustrated in Fig. 4c and Extended Data Fig. 7, the fitting of their energies at ν = 1/3, 2/3, 2/5 and 3/5 reveals an excellent linear scaling to $E_{\mathrm{c}}/|2p+1|$, and the fitted energy is close to zero as p increases (ν approaches 1/2). The results clearly corroborate that these modes have the same magnetoroton nature. Additionally, similar to the case at ν = 1/3, the mode intensities at ν = 2/3, 2/5 and 3/5 quickly collapse at elevated temperatures (Extended Data Fig. 9). The sensitivity of the modes on filling factors and temperature not only is consistent with the long-wavelength magnetoroton feature, but also reveals that the quantum metric dynamics that lead to the spin-2 geometry effect emerge from correlation.

In conclusion, our findings confirm that long-wavelength magnetorotons are chiral spin-2 modes in the FQH states. As summarized in Extended Data Table 1, the experimental observations incorporate key elements of CGMs characterized by their specific gaps ("masses"), chiral and spin-2 properties. In this light, our results provide evidence for emergent CGMs in the FQH liquids. Moreover, our measurements give crucial support to the new geometrical degree of freedom and offer opportunities to investigate exotic physics in the FQH effect from the aspect of quantum geometry, e.g., cyclotron graviton modes[20], nematic quantum Hall states[12,13,17,36] and partons[8,19,20]. In particular, the CP-RILS method provides a powerful way to identify the nature of the v = 5/2 state[7,18], known for its potential applications in topological quantum computation. Intriguingly, the study uncovers non-negligible quantum metric effects in the topological order, facilitating explorations of the interplay between geometry and correlation in a wide range of quantum systems including atomic layers[40,41], Kitaev lattices[22], cold atoms[42] and excitonic liquids[43].

References

1 Tsui, D. C., Stormer, H. L. & Gossard, A. C. Two-dimensional magnetotransport in the extreme quantum limit. *Phys. Rev. Lett.* **48**, 1559-1562 (1982).

2 Haldane, F. D. M. Geometrical description of the fractional quantum Hall effect. *Phys. Rev. Lett.* **107**, 116801 (2011).

3 Yang, B., Hu, Z.-X., Papić, Z. & Haldane, F. D. M. Model wave functions for the collective modes and the magnetoroton theory of the fractional quantum hall effect. *Phys. Rev. Lett.* **108**, 256807 (2012).

4 Son, D. T. Newton-Cartan geometry and the quantum Hall effect. *Preprint at https://arxiv.org/abs/1306.0638* (2013).

5 Golkar, S., Nguyen, D. X. & Son, D. T. Spectral sum rules and magneto-roton as emergent graviton in fractional quantum Hall effect. *J. High Energy Phys* **021** (2016).

6 Liou, S.-F., Haldane, F. D. M., Yang, K. & Rezayi, E. H. Chiral gravitons in fractional quantum hall liquids. *Phys. Rev. Lett.* **123**, 146801 (2019).

7 Nguyen, D. X. & Son, D. T. Probing the spin structure of the fractional quantum Hall magnetoroton with polarized Raman scattering. *Phys. Rev. Res.* **3**, 023040 (2021).

8 Nguyen, D. X., Haldane, F. D. M., Rezayi, E. H., Son, D. T. & Yang, K. Multiple magnetorotons and spectral sum rules in fractional quantum hall systems. *Phys. Rev. Lett.* **128**, 246402 (2022).

9 Girvin, S. M., MacDonald, A. H. & Platzman, P. M. Collective-excitation gap in the fractional quantum Hall effect. *Phys. Rev. Lett.* **54**, 581-583 (1985).

10 Pinczuk, A., Dennis, B. S., Pfeiffer, L. N. & West, K. Observation of collective excitations in the fractional quantum Hall effect. *Phys. Rev. Lett.* **70**, 3983-3986 (1993).

11 Yang, K. Geometry of compressible and incompressible quantum Hall states: Application to anisotropic composite-fermion liquids. *Phys. Rev. B* **88**, 241105 (2013).

12 Maciejko, J., Hsu, B., Kivelson, S. A., Park, Y. & Sondhi, S. L. Field theory of the quantum Hall nematic transition. *Phys. Rev. B* **88**, 125137 (2013).

13 You, Y., Cho, G. Y. & Fradkin, E. Theory of nematic fractional quantum hall states. *Phys. Rev. X* **4**, 041050 (2014).

14 Luo, X., Wu, Y.-S. & Yu, Y. Noncommutative Chern-Simons theory and exotic geometry emerging from the lowest Landau level. *Phys. Rev. D* **93**, 125005 (2016).

15 Johri, S., Papić, Z., Schmitteckert, P., Bhatt, R. N. & Haldane, F. D. M. Probing the geometry of the Laughlin state. *New J. Phys.* **18**, 025011 (2016).

16 Gromov, A. & Son, D. T. Bimetric theory of fractional quantum hall states. *Phys. Rev. X* **7**, 041032 (2017).

17 Yang, B. Microscopic theory for nematic fractional quantum hall effect. *Phys. Rev. Res.* **2**, 033362 (2020).

18 Haldane, F. D. M., Rezayi, E. H. & Yang, K. Graviton chirality and topological order in the half-filled landau level. *Phys. Rev. B* **104**, L121106 (2021).

19 Balram, A. C., Liu, Z., Gromov, A. & Papić, Z. Very-high-energy collective states of partons in fractional quantum hall liquids. *Phys. Rev. X* **12**, 021008 (2022).

20 Wang, Y. & Yang, B. Geometric fluctuation of conformal Hilbert spaces and multiple graviton modes in fractional quantum Hall effect. *Nat. Commun.* **14**, 2317 (2023).

21 Kirmani, A. *et al.* Probing geometric excitations of fractional quantum hall states on quantum computers. *Phys. Rev. Lett.* **129**, 056801 (2022).

22 Farjami, A., Horner, M. D., Self, C. N., Papić, Z. & Pachos, J. K. Geometric description of the Kitaev honeycomb lattice model. *Phys. Rev. B* **101**, 245116 (2020).

23 Gianfrate, A. *et al.* Measurement of the quantum geometric tensor and of the anomalous Hall drift. *Nature* **578**, 381-385 (2020).

24 Gao, A. *et al.* Quantum metric nonlinear Hall effect in a topological antiferromagnetic heterostructure. *Science* **381**, 181-186 (2023).

25 Wang, N. *et al.* Quantum-metric-induced nonlinear transport in a topological antiferromagnet. *Nature* **621**, 487-492 (2023).

26 Jain, J. K. *Composite fermions*. (Cambridge University Press, 2007).

27 Davies, H. D. M., Harris, J. C., Ryan, J. F. & Turberfield, A. J. Spin and Charge Density Excitations and the Collapse of the Fractional Quantum Hall State at $\nu = 1/3$. *Phys. Rev. Lett.* **78**, 4095-4098 (1997).

28 Kang, M., Pinczuk, A., Dennis, B. S., Pfeiffer, L. N. & West, K. W. Observation of Multiple Magnetorotons in the Fractional Quantum Hall Effect. *Phys. Rev. Lett.* **86**, 2637-2640 (2001).

29 Scarola, V. W., Park, K. & Jain, J. K. Rotons of composite fermions: Comparison between theory and experiment. *Phys. Rev. B* **61**, 13064-13072 (2000).

30 Platzman, P. M. & He, S. Resonant Raman scattering from mobile electrons in the fractional quantum Hall regime. *Phys. Rev. B* **49**, 13674-13679 (1994).

31 Fierz, M. & Pauli, W. On relativistic wave equations for particles of arbitrary spin in an electromagnetic field. *Proc. R. Soc. London, Ser. A* **173**, 211-232 (1939).

32 Bergshoeff, E. A., Hohm, O. & Townsend, P. K. Massive gravity in three dimensions. *Phys. Rev. Lett.* **102**, 201301 (2009).

33 Bergshoeff, E. A., Rosseel, J. & Townsend, P. K. Gravity and the Spin-2 Planar Schrödinger Equation. *Phys. Rev. Lett.* **120**, 141601 (2018).

34 Kang, M. *et al.* Inelastic Light Scattering by Gap Excitations of Fractional Quantum Hall States at $1/3 \leqslant \nu \leqslant 2/3$. *Phys. Rev. Lett.* **84**, 546-549 (2000).

35 Wurstbauer, U., West, K. W., Pfeiffer, L. N. & Pinczuk, A. Resonant inelastic light scattering investigation of low-lying gapped excitations in the quantum fluid at $\nu = 5/2$. *Phys. Rev. Lett.* **110**, 026801 (2013).

36 Du, L. *et al.* Observation of new plasmons in the fractional quantum Hall effect: Interplay of

topological and nematic orders. *Sci. Adv.* **5**, eaav3407 (2019).

37 Liu, Z. *et al.* Domain textures in the fractional quantum Hall effect. *Phys. Rev. Lett.* **128**, 017401 (2022).

38 Halperin, B. I., Lee, P. A. & Read, N. Theory of the half-filled Landau level. *Phys. Rev. B* **47**, 7312-7343 (1993).

39 Simon, S. H. & Halperin, B. I. Finite-wave-vector electromagnetic response of fractional quantized Hall states. *Phys. Rev. B* **48**, 17368-17387 (1993).

40 Park, H. *et al.* Observation of fractionally quantized anomalous Hall effect. *Nature* **622**, 74-79 (2023).

41 Zeng, Y. *et al.* Thermodynamic evidence of fractional Chern insulator in moiré $MoTe_2$. *Nature* **622**, 69-73 (2023).

42 Léonard, J. *et al.* Realization of a fractional quantum Hall state with ultracold atoms. *Nature* **619**, 495-499 (2023).

43 Wang, R., Sedrakyan, T. A., Wang, B., Du, L. & Du, R.-R. Excitonic topological order in imbalanced electron–hole bilayers. *Nature* **619**, 57-62 (2023).

Main figure legends

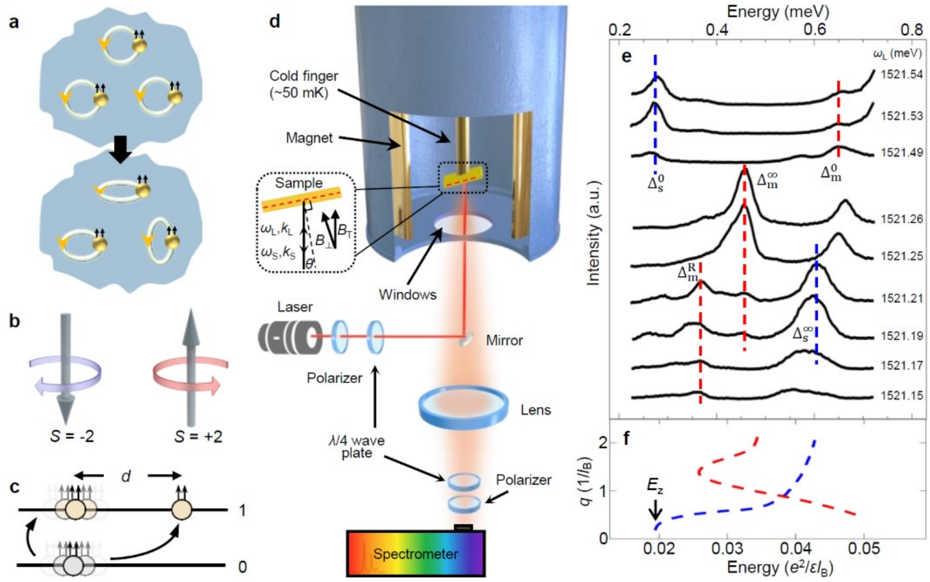

Fig. 1. **Graviton modes and inelastic light scattering. a,** The cartoon representation describes the dynamics of the internal metric. At $\nu = 1/3$, each CF moves in a circular orbit and the spatially dependent metric could be phenomenologically considered to deform the shape of CF orbits. **b**, Depiction of the chiral spin-2 characteristic of CGMs. In FQH states around $\nu = 1/2$, CGMs of electron states carry angular momentum $S = -2$ while those of the particle-hole conjugates exhibit the reversed chirality with $S = +2$. **c**, At $\nu = 1/3$, CFs are excited from the topmost occupied CF Landau level to the next empty one. As the distance d between each CF (yellow) and its quasihole (grey) approaches zero, CGMs are triggered by metric fluctuations. **d**, The experimental setup for RILS performed in a dilution refrigerator. Two polarizers are used to generate orthogonal linear polarizations of incident and scattered lights in the unpolarized geometry. In CP-RILS, additional $\lambda/4$ wave plates are positioned after the laser and in front of the spectrometer to generate and detect CP lights. Inset: A depiction of the backscattering geometry at a tilted angle θ. Incident and scattered lights have energies ω_L and ω_S with wavevectors k_L and k_S, respectively. The total magnetic field B_T and its perpendicular component $B_\perp$ are shown. **e**, RILS spectra at $\nu = 1/3$ in the unpolarized geometry with $\theta = 25°$. Red and blue dashed lines indicate magnetoroton and spin-wave excitations, respectively. **f**, Calculated dispersions of collective excitations at $\nu = 1/3$. The red dashed line is scaled down from the ideal zero-width result of magnetoroton modes[29] by a constant of 0.33 to account for the finite-thickness effect. E_Z is the Zeeman energy. The blue dashed line represents a generic dispersion of spin-wave excitations.

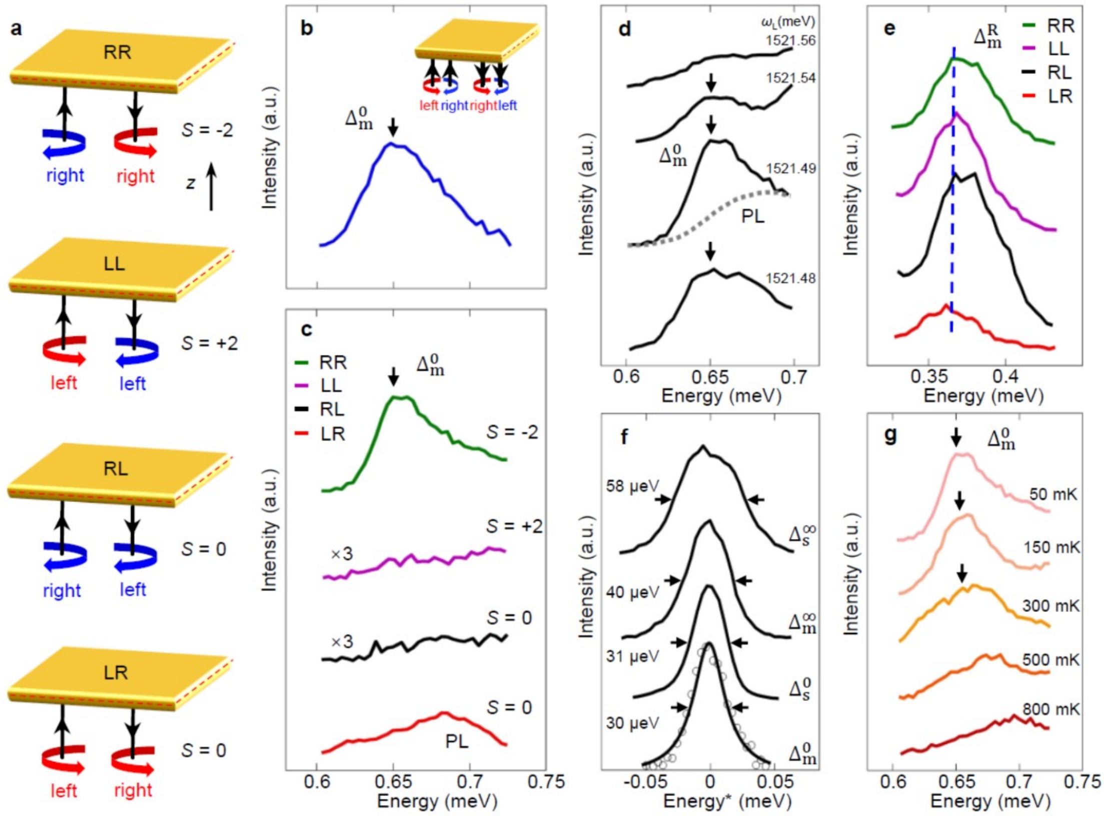

Fig. 2. **CP-RILS measurements at ν = 1/3 with θ = 25°. a**, CP-RILS geometries are depicted. Right (left) handedness represents right- (left-) CP photons, defined as clockwise (anticlockwise) rotation of the electric field vector in a plane from the point of view of the receiver. Blue (red) curved arrows indicate incident or scattered photons with spin -1 (+1) in the magnetic field (z) direction. The transferred spin to the FQH liquid is marked for each geometry. **b**, RILS spectrum of Δ_m^0 at resonance in the unpolarized geometry at ν = 1/3. The incident and scattered lights contain both left- and right-circular-polarized photons. We note that this mode does not emerge at other resonances throughout the entire range of investigated incident photon energies. **c**, Δ_m^0 spectra in four CP geometries at ν = 1/3 with the same incident photon energy as that in **b**. RILS peaks are marked by vertical black arrows. The signals in LR are attributed to PL background (Supplementary Fig. 1). Spectral intensities in LL and RL are multiplied by a factor of 3. **d**, Resonant enhancement of RILS signals of Δ_m^0 in RR. The dashed line represents the smoothed PL background in this geometry. **e**, Δ_m^R spectra in four CP geometries. RILS peaks are marked by the blue dashed line. In contrast to Δ_m^0, Δ_m^R does not possess a specific chirality[5,7]. The RILS peak in LR is weak, since weak PL background affects the resonant enhancement. **f**, FWHM of several collective modes in RR. Values of FWHM are displayed. Energy* refers to normalized energy with the peak energy set zero. Open dots for Δ_m^0 are experimental data with PL background subtracted (Extended Data Fig. 2), which are fitted with a Lorentzian peak. **g,** Marked temperature dependence of Δ_m^0 in RR.

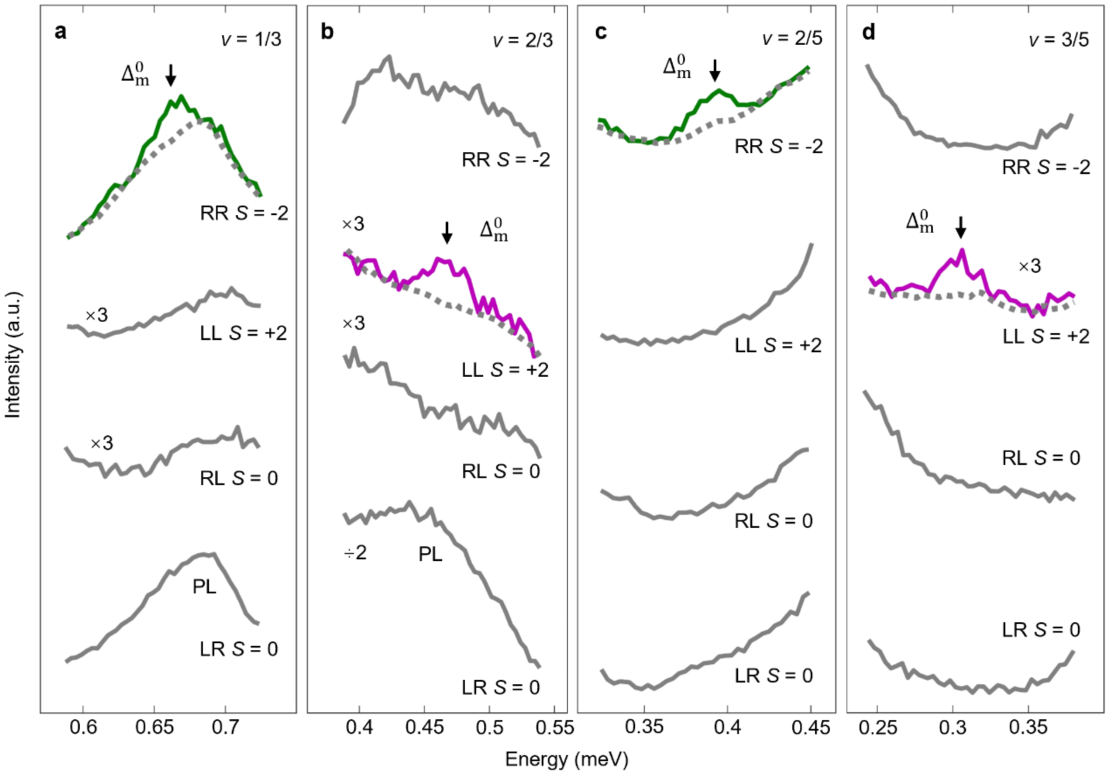

Fig. 3. **Circular polarization dependence of the $\mathbf{\Delta_m^0}$ modes in FQH states with θ = 10°.** At extremely small kl_B, Δ_m^0 spectra in four CP geometries are displayed: **a** for v = 1/3, **b** for v = 2/3, **c** for v = 2/5, and **d** for v = 3/5. At v = 1/3 and 2/5, the Δ_m^0 modes are observable in the RR geometry (marked by arrows in green spectra), while at v = 2/3 and 3/5, the modes are found in the LL geometry (marked by arrows in purple spectra). Grey dashed lines represent smoothed PL signals in the corresponding CP geometries. At these FQH states, the Δ_m^0 modes are absent in other geometries where PL signals contribute to the spectra intensities (shown in grey). Specifically, Extended Data Fig. 4b and Supplementary Fig. 4 show that the signals in the LR geometry in **a** and **b** are from PL background, respectively. For clarity, the spectra intensities in some geometries are rescaled as specified.

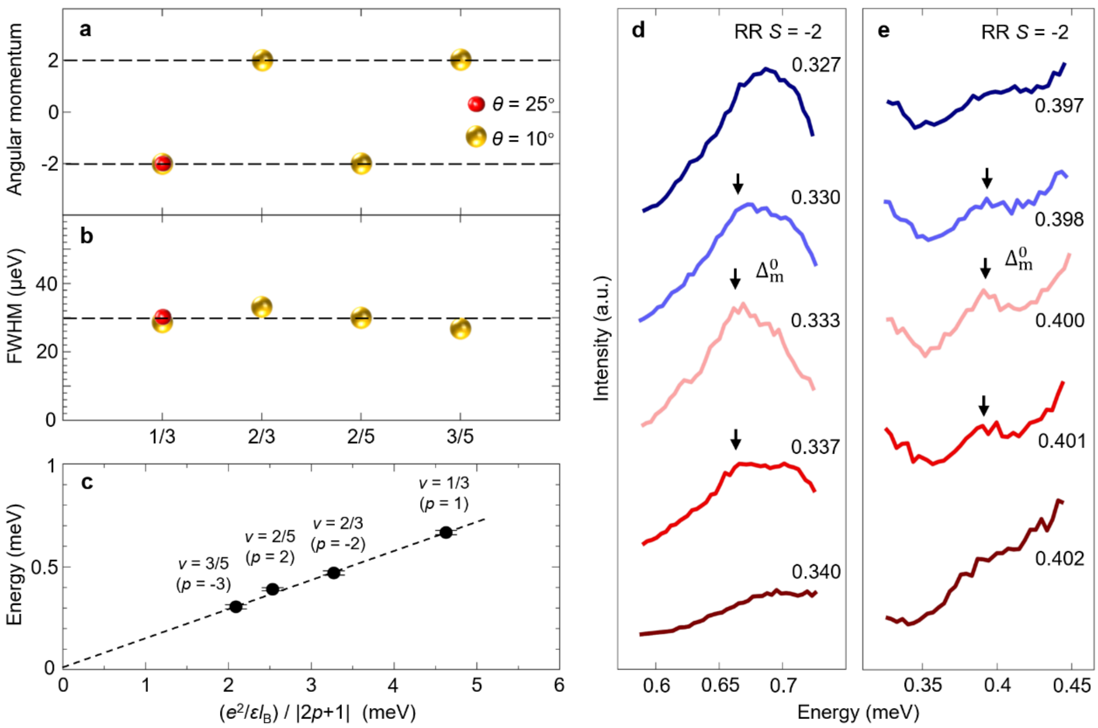

Fig. 4. **Chiral spin-2 long-wavelength magnetoroton modes in FQH states. a,** Angular momenta of the Δ_{m}^{0} modes at $\nu = 1/3$, 2/3, 2/5 and 3/5 with $\theta = 25°$ (red) and $\theta = 10°$ (gold). **b**, FWHM of the Δ_{m}^{0} modes in the FQH states with $\theta = 25°$ (red) and $\theta = 10°$ (gold). Dashed lines in **a** and **b** are guides to the eye. **c,** Energies of the Δ_{m}^{0} modes plotted against $(e^2/\varepsilon l_B)/|2p+1|$ at $\theta = 10°$. The error bars indicate the uncertainty in determining the energy positions in RILS spectra. The mode energies at $\nu = 1/3$ ($p = 1$), 2/5 ($p = 2$), 2/3 ($p = -2$) and 3/5 ($p = -3$) are found proportional to $(e^2/\varepsilon l_B)/|2p+1|$ very well. The dashed line is from the fitting with details available in Extended Data Fig. 7. **d** and **e** display the filling factor dependence of the Δ_{m}^{0} modes around $\nu = 1/3$ and 2/5 in the RR geometry, respectively. RILS peaks are marked by vertical black arrows.

Methods

Low-temperature optical measurements

The 2DEG is confined in a modulation-doped 58.5 nm GaAs single QW. The electron mobility at 300 mK in a sample from the same wafer reaches 14×10^{6} cm^2/Vs at density $n = 7.2\times10^{10}$ cm^{-2}. The ultra-high-mobility 2DEG under magnetic fields provides a clean platform to explore correlated many-body physics. The high sample quality enables RILS observations of collective modes of FQH states.

The sample is mounted on the cold finger of a ^{3}He/^{4}He dilution refrigerator (Bluefors LD400, base temperature of about 50 mK), which is inserted into the cold bore of a 14 T superconducting magnet. To ensure good thermal contact, the sample is attached to the cold finger using copper-loaded grease. Gold wires are connected from the QW to the copper finger to further enhance thermal contact with the 2DEG.

Optical windows are installed at the bottom of the dilution refrigerator to provide the direct optical access, as illustrated in Fig. 1d. In measurements, we employ a conventional backscattering geometry with a small tilt angle θ between the incident (scattered) photons and the normal of the sample surface[10,28,34,44]. We note that since the 2DEG is embedded within the QW, the refraction between the vacuum and the GaAs/AlGaAs-based QW with small θ renders the incident light nearly normal to the 2DEG plane. The perpendicular magnetic field applied to the sample is $B_{\perp} = B_{\mathrm{T}}\cos\theta$, where B_{T} represents the total magnetic field. For a different θ, B_{T} is adjusted to retain $B_{\perp}$ of the corresponding FQH state. A tunable Ti:sapphire laser is utilized and the incident photon power density is kept below 10^{-4} W/cm^2 to prevent significant heating of the sample at the base temperature. For unpolarized RILS measurements that suppress parasitic reflected lights at the laser wavelength, a linear polarizer is used to rotate the light polarization so that the incident linearly-polarized light becomes perpendicular to the scattered linearly-polarized light and the direction of the entrance slit in the spectrometer[45]. As shown in Supplementary Fig. 6a, scattered lights are collected by lenses and focused onto the entrance slit of the spectrometer. Another linear polarizer, aligned parallel to the entrance slit, is placed in front of the spectrometer to improve the selectivity for polarized lights. In the case of CP-RILS measurements (Supplementary Fig. 6b), additional $\lambda/4$ wave plates are inserted behind the linear polarizer and in front of the spectrometer to generate CP lights and convert CP lights to linearly polarized lights, respectively. We use a triple grating spectrometer equipped with holographic gratings to disperse and record the scattered signals. Photons are detected with a charged coupled device with a liquid nitrogen cooling system, offering a high spectral resolution with low readout noise. The system achieves a high combined spectral resolution < 16 μeV. Compared with the case at 25°, we narrow down the entrance slit of the spectrometer at 10° to mitigate a stronger stray light effect. This adjustment, while necessary, also results in a general suppression of the observed intensities of the scattered lights.

Spectra are displayed as a function of energy difference $\omega = \omega_{\mathrm{L}} - \omega_{\mathrm{S}}$, where ω_{L} is the incident photon energy and ω_{S} is the scattered photon energy. In this framework, RILS spectra are obtained by tuning ω_{L} to the resonance conditions. Low-lying RILS peaks do not shift with ω, distinguishing them from PL bands. In RILS experiments, a small wavevector k is transferred from photons to the sample, $k = (2\omega_{\mathrm{L}}/c)\sin\theta \approx 2.67\times10^{6}$ m^{-1} at $\theta = 10^{\circ}$. In this case, $k \approx 0.02/l_{\mathrm{B}}$ enables long-wavelength excitations with $q = k$ under wavevector conservation. In our experiments at $\nu = 1/3$, k can be tuned from ≈ 0.02 to ≈ 0.05. At larger wavevectors, i.e., $0.05 < kl_{\mathrm{B}} < 0.1$, the magnetoroton was found to split into two peaks[44] that might be attributed[5,7,37] to mixed modes comprising spin +2 and spin -2. Additionally, weak residual disorder could break wavevector conservation, allowing RILS to probe modes with $ql_B \gtrsim 1$ in the magnetoroton dispersion[27,28,45]. We determine the magnetic field for $\nu = 1$ which establishes the filling factor dependence of the magnetic fields (see below).

Determination of filling factors

Filling factors of FQH states in the lowest Landau level are determined from RILS measurements of the long-wavelength spin-wave modes Δ_S^0 around $\nu = 1$. The modes are exclusively at the Zeeman energy E_Z. Significant enhancement of the Δ_S^0 mode is expected at $\nu = 1$ when the magnetic field is tuned to define this fully spin polarized state[46]. The determination of the magnetic field strength at $\nu = 1$ enables the accurate calculation of magnetic fields for other filling factors.

Supplementary Figure 7 presents the RILS spectrum of the Δ_S^0 mode under maximized resonance enhancement at $\nu = 1$, which is obtained in the unpolarized geometry. It is worth noting that the very sharp spin-wave mode at $\nu = 1$ is observed only under extreme resonance conditions. The very intense spin-wave peak completely disappears when the incident photon energy is tuned away by approximately 95 μeV.

Supplementary Figure 7 illustrates that a deviation of the filling factor from $\nu = 1$ significantly reduces the mode intensity. Specifically, a small deviation in filling factor of $\Delta\nu = \pm 0.01$ from $\nu = 1$ results in a reduction of the mode intensity by about 5% and a change of $\Delta\nu = \pm 0.02$ from $\nu = 1$ leads to a decrease of the intensity by more than 10%. This reduction is due to decreased spin polarization[46] as the filling factor is away from $\nu = 1$. Following this procedure, we can precisely determine the magnetic field for $\nu = 1$ based on the spin-wave mode intensity in RILS measurements. Consequently, the accurate filling factor can be identified as a function of magnetic fields in the lowest Landau level. In our measurement, the magnetic field for $\nu = 1$ is found to be 3.6 T at $\theta = 25°$ and correspondingly, the electron density of the investigated sample yields $n = 7.9\times10^{10}$ cm^{-2}. The case at $\theta = 10°$ is similar.

Identification of collective modes

Figure 1e presents RILS spectra from intra-Landau-level collective excitations at $\nu = 1/3$ in the unpolarized geometry with $\theta = 25°$. RILS peaks, observed at E_Z (at $\nu = 1/3$ and other filling factors), are identified as the long-wavelength spin-wave mode Δ_S^0 (ref. 10). The Δ_S^0 mode determined by the Zeeman energy suggests that the wavevector is conserved in the light scattering process ($q = k \ll 1/l_B$) and thus the mode is in the long-wavelength limit. Wavevector conservation is further confirmed by its sharp peak[10]. We mention that the similar peak sharpness of the spin-2 mode and Δ_S^0, as illustrated in Fig. 2f, indicates that wavevector conservation also applies to the spin-2 mode, placing it in the long-wavelength limit with $q = k \ll 1/l_B$. Moreover, a broader mode observed at 0.6 meV persists to non-FQH filling factors (e.g., $\nu = 0.3$ and 0.38) and is insensitive to temperature up to 800 mK at $\nu = 1/3$, suggesting that it is the large-q spin-wave excitation Δ_S^∞ activated by disorder scattering[27,45].

In contrast, we identify three other low-lying modes in Fig. 1e, which vanish with increasing temperatures below 800 mK (as shown in Extended Data Figs. 1b, 1d and 1f) and quickly collapse for filling factors away from $\nu = 1/3$ (as shown in Extended Data Figs. 1a, 1c and 1e). The characteristic temperature and filling factor dependence suggest that they are collective magnetoroton excitations of the FQH liquid[10,27]. At $\nu = 1/3$, there are three characteristic features in the magnetoroton dispersion: the roton minimum $\Delta_{\mathrm{m}}^{\mathrm{R}}$, the magnetoroton $\Delta_{\mathrm{m}}^{\infty}$ at large wavevectors and the long-wavelength magnetoroton Δ_{m}^{0}. $\Delta_{\mathrm{m}}^{\mathrm{R}}$ can be understood as a quasiparticle-quasihole pair and has been observed. $\Delta_{\mathrm{m}}^{\infty}$ corresponds to the activation gap in transport and has been studied intensively. Δ_{m}^{0} is linked to the macroscopic coherence and the predicted CGMs, but its understanding is far from complete.

Then we compare the experimental results with the calculated dispersion scaled down by a constant from the ideal 2D result[29] (the dashed red line of Fig. 1f), to facilitate specific assignments of the observed modes. Within the three modes, the mode at the highest energy (0.65 meV) is interpreted as Δ_{m}^{0}. The modes at 0.36 meV and 0.45 meV are ascribed to $\Delta_{\mathrm{m}}^{\mathrm{R}}$ and $\Delta_{\mathrm{m}}^{\infty}$, respectively. The observed energies are smaller than those measured in the $\nu = 1/3$ state host in narrow QWs, due to larger finite-thickness effects that soften short-range Coulomb interactions[9,10,29,47]. The softened interactions would lower energies of the magnetoroton modes. Remarkably, the scaled constants that account for finite-thickness effects are found close across various FQH states, as shown in Fig. 1f, Extended Data Fig. 3b, Supplementary Figs. 3b and 5b.

Furthermore, at $kl_{\mathrm{B}} \approx 0.05$, the energy ratio of Δ_{m}^{0} to $\Delta_{\mathrm{m}}^{\mathrm{R}}$ in our experiments shows a discrepancy as large as 20%, compared to theoretical calculations at $q \approx 0$ (in the expected range from 2.02 to 2.27). We attribute it to the effect of the relatively large wavevector[29,45]. As shown in Extended Data Fig. 5, at a smaller wavevector ($kl_{\mathrm{B}} \approx 0.02$), this discrepancy is greatly suppressed and the observed ratio falls within the expected range. Such agreement in mode energies is remarkable and confirms our assignments.

Alternative explanations

Theories[9,48,49] suggest that at $\nu = 1/3$ two $\Delta_{\mathrm{m}}^{\mathrm{R}}$ with opposite momenta might form a two-roton bound state with zero (total) momentum. The energy ratio of the two-roton state to $\Delta_{\mathrm{m}}^{\mathrm{R}}$ is expected[48,49] to be below two (specifically 1.8 at $k \approx 0$) and to increase with larger k. In our experiments, at $\nu = 1/3$, the energy ratio of the spin-2 mode to $\Delta_{\mathrm{m}}^{\mathrm{R}}$ reaches 2.07 at $kl_{\mathrm{B}} \approx 0.02$ and decreases by 15% at $kl_{\mathrm{B}} \approx 0.05$, as shown in Extended Data Fig. 5. Apparently, the observed mode behaviors are distinct from the expectation for the two-roton state. Similarly, at $\nu = 2/3$, the observed energy ratio of the spin-2 mode to $\Delta_{\mathrm{m}}^{\mathrm{R}}$ about 2.2 at $\nu = 2/3$ (Extended Data Fig. 5) notably surpasses that predicted for the two-roton bound state, again ruling out the latter as a plausible explanation.

In previous theoretical treatments of the single mode approximation[9,30], the intensity of Δ_{m}^{0} would be associated with the dynamical structure factor in the lowest Landau level; it is expected to vanish quickly with $(kl_{\mathrm{B}})^4$, in accordance with Kohn's theorem which claims that the cyclotron mode exhausts the dipole spectral weight at long wavelength. For kl_{B} reduced by a factor of 2.5, the Δ_{m}^{0} intensity would be suppressed by a factor of $\approx 1/40$, causing the mode to be optically invisible. However, in our experiments, the measured intensities of Δ_{m}^{0} remain comparable (Figs. 2c and 3a), which cannot be explained by this dipole picture.

Resonant enhancement of inelastic light scattering

Collective excitations of FQH liquids are delicate emergent phenomena which can be observed by RILS[10]. It is achieved by tuning ω_L to the resonance conditions. Resonant enhancements occur when the photon energy matches intermediate inter-band optical transitions that involve conduction and valence bands of the GaAs QW. Under a strong magnetic field, the complex structure of Landau levels in valence bands modifies optical matrix elements[50].

RILS by collective excitations can be described using 3rd order time-dependent perturbation theory. Three virtual transitions are involved: In the first step, through light-matter interactions H_{ep} an incident photon of energy ω_L is annihilated, promoting an electron from a valence band state $|v\rangle$ to an intermediate state $|m\rangle$ which is in a conduction band. ω_m is the energy of the transition from $|v\rangle$ to $|m\rangle$. In the second step, electron-electron interactions H_{ee} cause the scattering from $|m\rangle$ to the second intermediate state $|n\rangle$. A collective mode (quasiparticle) of the electron liquid is created and coupled to such scattering. In the third step, the recombination of the final conduction $|n\rangle$ and valence states $|v\rangle$ emits a scattered photon with energy ω_S. The transition from $|n\rangle$ to $|v\rangle$ has energy ω_n. Due to energy conservation, the energy of the collective mode probed in RILS is given by the energy shift during the light scattering $\omega = \omega_L - \omega_S$. The three-step process and the scattering intensity can be written as[51]:

$$I(\omega) \propto \left|\sum_{m,n} \frac{\langle v|H_{\mathrm{ep}}|n\rangle\langle n|H_{\mathrm{ee}}|m\rangle\langle m|H_{\mathrm{ep}}|v\rangle}{(\omega_{\mathrm{s}}-\omega_{\mathrm{n}})(\omega_{\mathrm{L}}-\omega_{\mathrm{m}})}\right|^2$$

where we find a maximized light scattering intensity at resonance conditions, i.e., when the denominator in the above expression is vanishingly small. In our experiments, when the intermediate inter-band optical transitions from $|n\rangle$ to $|v\rangle$ overlap PL transitions of *X*, RILS is enhanced by the resonance with *X* transitions[51]. As more *X* transitions are involved, which give stronger PL signals, the scattering intensity would be expected larger. The strength of the PL background in different circular polarization setups depends on the relevant optical transitions between conduction-band and valence-band Landau levels. We have to mention that although the strength of PL background affects the resonant enhancement of RILS peaks, the appearance of RILS peaks is determined by the presence of a collective mode, not by the strength of PL background.

Method references

44 Hirjibehedin, C. F. *et al.* Splitting of long-wavelength modes of the fractional quantum Hall liquid at $\nu = 1/3$. *Phys. Rev. Lett.* **95**, 066803 (2005).

45 Rhone, T. D. *et al.* Higher-energy composite fermion levels in the fractional quantum Hall effect. *Phys. Rev. Lett.* **106**, 096803 (2011).

46 Gallais, Y., Yan, J., Pinczuk, A., Pfeiffer, L. N. & West, K. W. Soft Spin Wave near $\nu = 1$: Evidence for a Magnetic Instability in Skyrmion Systems. *Phys. Rev. Lett.* **100**, 086806 (2008).

47 Zhang, F. C. & Sarma, S. D. Excitation gap in the fractional quantum Hall effect: Finite layer thickness corrections. *Phys. Rev. B* **33**, 2903-2906 (1986).

48 Park, K. & Jain, J. K. Two-roton bound state in the fractional quantum Hall effect. *Phys. Rev. Lett.* **84**, 5576-5579 (2000).

49 Ghosh, T. K. & Baskaran, G. Modeling two-roton bound state formation in the fractional quantum Hall system. *Phys. Rev. Lett.* **87**, 186803 (2001).

50 Goldberg, B. B. *et al.* Optical transmission spectroscopy of the two-dimensional electron gas in

GaAs in the quantum hall regime. *Phys. Rev. B* **38**, 10131-10134 (1988).
51 Hirjibehedin, C. F. *et al.* Resonant enhancement of inelastic light scattering in the fractional quantum Hall regime at $\nu = 1/3$. *Solid State Commun.* **127**, 799-803 (2003).

Acknowledgements

We gratefully acknowledge illuminating discussions with Bo Yang, Dung Xuan Nguyen, Dam Thanh Son, Kun Yang, Jainendra K. Jain and Rui-Rui Du. We thank Bo Yang for comments on the manuscript. We thank Yifan Wang and Xinyu Lu for assistance in low-temperature measurements. This work is supported by the National Natural Science Foundation of China (Grant No. 12074177), Innovation Program for Quantum Science and Technology (Grant No. 2021ZD0302600), Program for Innovative Talents and Entrepreneur in Jiangsu and the start-up funding of Nanjing University. The work at Columbia University is funded by the National Science Foundation, Division of Materials Research under Grant DMR-2103965. The Princeton University portion of this research is funded in part by the Gordon and Betty Moore Foundation's EPiQS Initiative, Grant GBMF9615.01 to Loren Pfeiffer. U. W. acknowledges support from German Science Foundation under Grants WU 637/7-1 and 7-2.

Author contributions

L. D. supervised the project, L. D. and J. L. designed and set up the low-temperature optical facility, L. D. and Z. L. conceived the experiments, K. W. W. and L. N. P. grew the heterostructure, J. L., Z. L., Z. Y., Y. H. and L. D. performed the optical measurements, L. D., J. L., Z. L. and Z. Y. analyzed the data, A. P., Z. L., U. W. and L. D. discussed the scientific objectives, L. D., Z. L. and J. L. wrote the paper. J. L., Z. L., Z. Y., U. W., C. R. D. and L. D. commented on the paper during the writing process.

Competing interests

The authors declare no competing interests.

Additional information

Supplementary information The online version contains supplementary material available online.

Correspondence and requests for materials should be addressed to Lingjie Du.

Reprints and permission information is available online.

Data availability

All data needed to evaluate the conclusions in the paper are included in this paper. Additional data that support the plots and other analysis in this work are available from the corresponding author upon request.

Extended data figure legends

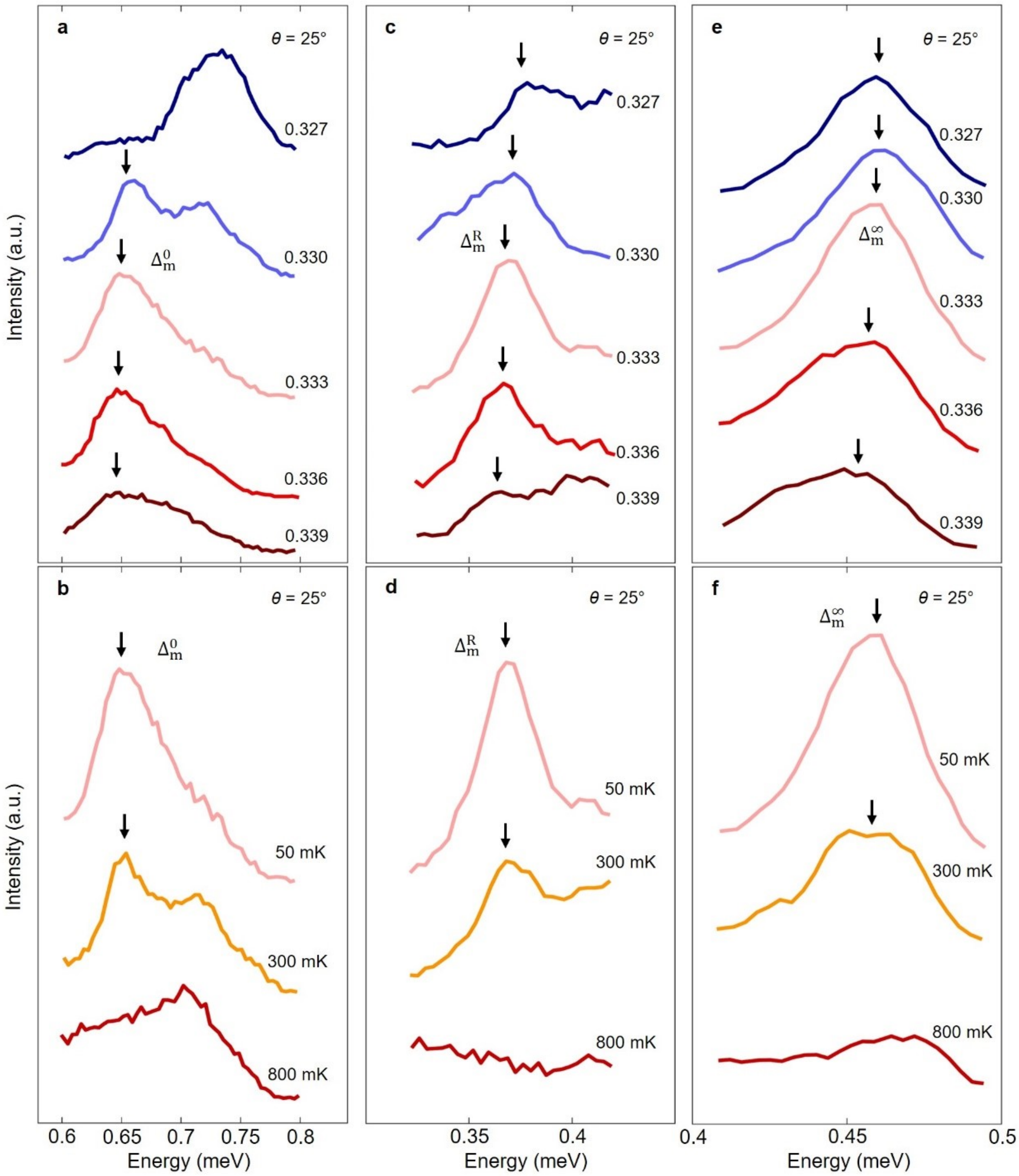

Extended Data Fig. 1. **Filling factor and temperature dependence of magnetoroton modes at *ν* = 1/3 in the unpolarized geometry with *θ* = 25°.** Spectra of Δ_m^0, Δ_m^R and Δ_m^∞ at filling factors around $\nu = 1/3$ are shown in **a**, **c** and **e**, respectively. The mode intensities reach their maxima at $\nu = 1/3$, and rapidly decrease as filling factors deviate from $\nu = 1/3$. The observations suggest that as the system becomes more compressible, the quantum liquid supporting magnetoroton excitations appears to vanish. Temperature dependence of Δ_m^0, Δ_m^R and Δ_m^∞ at $\nu = 1/3$ is shown in **b, d** and **f**, respectively. With increased temperatures, the intensities of the magnetoroton modes decrease and vanish at temperatures below 800 mK. The behaviors indicate that the magnetoroton modes are highly temperature-sensitive collective excitations, further highlighting their roles in characterizing the properties of the FQH states. RILS peaks are marked by vertical black arrows.

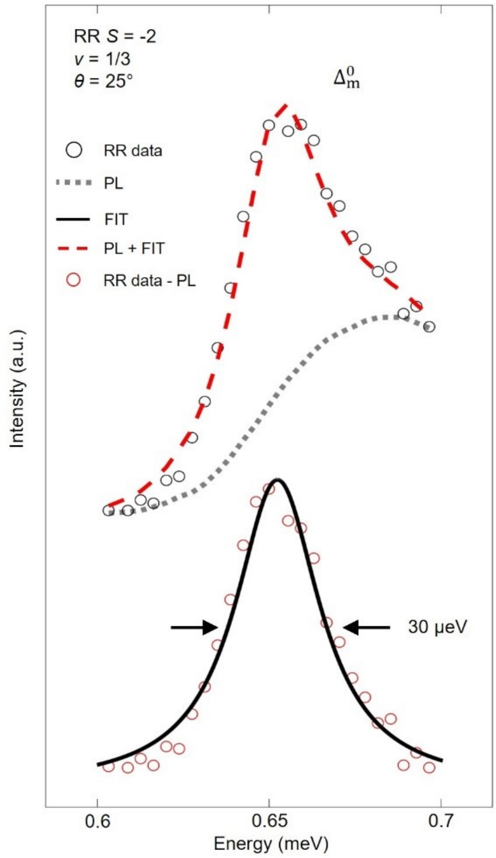

Extended Data Fig. 2. **Peak fitting of the Δ_m^0 mode at ν = 1/3 in the RR geometry with θ = 25°.** The measured Δ_m^0 mode at resonance (black open dots) includes contribution from PL background. The red open dots show the Δ_m^0 mode after subtracting smoothed PL background (the grey dashed line), which are fitted by a Lorentzian peak (the black line) with FWHM of 30 μeV. The combination (the red dashed line) of the fitted Lorentzian peak and PL background gives a remarkable match with the measured signals in the RR geometry. The relatively narrow peak width of this mode suggests wavevector conservation in the scattering process with $q = k \ll 1/l_B$, confirming its long-wavelength nature.

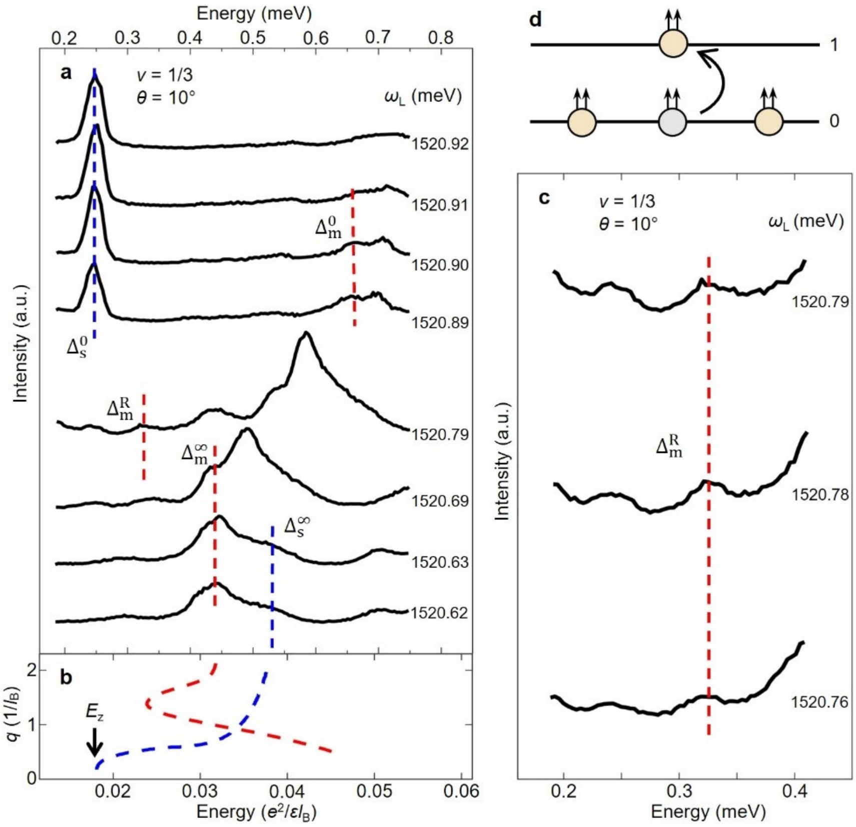

Extended Data Fig. 3. **RILS measurements at *ν* = 1/3 with *θ* = 10°. a,** RILS spectra at *ν* = 1/3 in the unpolarized geometry as a function of ω_L. Similar to those in Fig. 1e, the red and blue dashed lines indicate magnetoroton and spin-wave excitations, respectively. Compared with the result at $\theta = 25^o$, Δ_s^0 at $\theta = 10°$ has a lower energy but remains at E_z, confirming its assignment. **b,** Calculated dispersions of collective excitations at *ν* = 1/3 that support the assignment of the modes. The red dashed line is scaled down from the ideal zero-width result[29] by a factor of 0.305, accounting for the finite-thickness effect. The blue dashed line represents a generic dispersion for the spin-wave excitations. **c,** RILS spectra of the Δ_m^R excitation at *ν* = 1/3 in the unpolarized geometry at different ω_L. The well-resolved peaks are marked by the vertical red dashed line. We mention that the Δ_m^R mode energy at 25° is larger than that at 10°, since a larger tilted angle induces a higher in-plane magnetic field, causing the electrons to behave in a more 2D manner. On the other hand, the Δ_m^0 energies at two tilted angles are closed. It is because a smaller tilted angle also gives a reduced kl_B in the magnetoroton dispersion, which corresponds to an increased Δ_m^0 energy, as shown in the red dashed line in **b**. The two factors interplay in the case of Δ_m^0. **d**, At *ν* = 1/3, magnetoroton modes could be understood as excitations of CFs from the topmost (the lowest) occupied CF Landau level to the next unoccupied one.

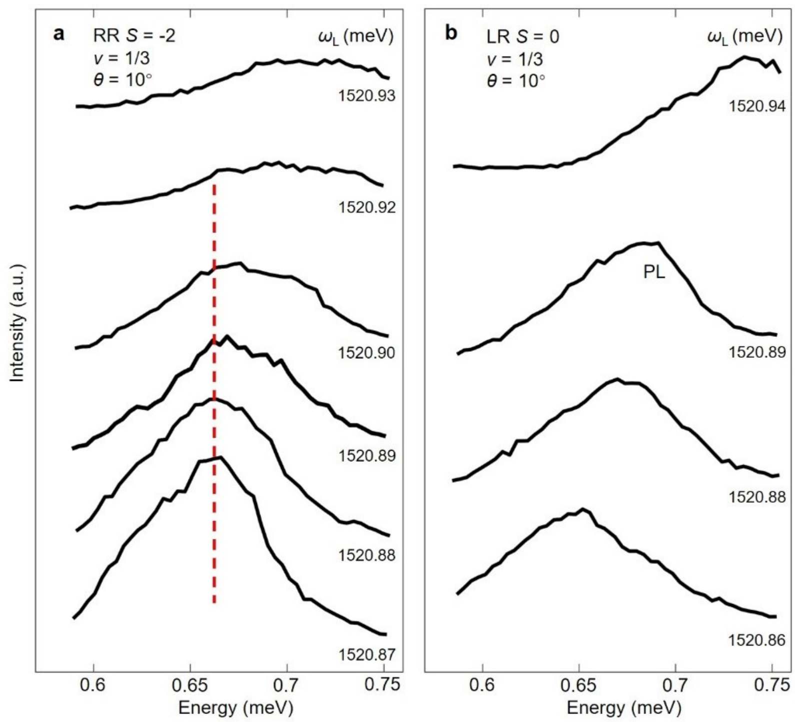

Extended Data Fig. 4. **Optical spectra at ν = 1/3 measured at different ω_L in the RR and LR geometries with θ = 10°**. **a**, Resonant enhancement of RILS signals of the Δ_m^0 mode in the RR geometry. The RILS peaks maintain a consistent energy shift at different ω_L. The resonant enhancement of Δ_m^0 is clearly demonstrated by the marked intensity dependence on ω_L. RILS peaks are marked by the dashed red line. **b**, Optical spectra measured in the LR geometry. The feature of the spectrum measured at ω_L = 1520.89 meV (that also appears in the LR geometry in Fig. 3a) shifts as ω_L varies, which is identified as PL signals. No RILS signals are found in the spectra in the LR geometry.

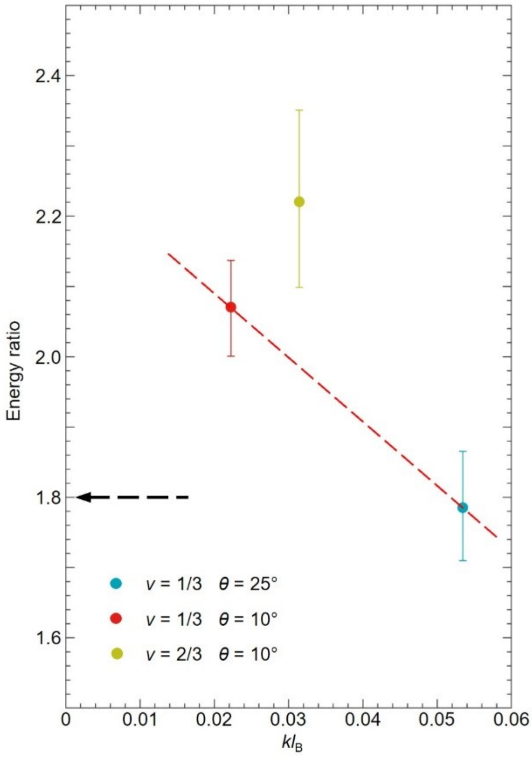

Extended Data Fig. 5. **Energy ratios of the measured spin-2 modes to Δ_m^R in the ν = 1/3 and 2/3 states.** In RILS experiments, the wavevector $k = (2\omega_L/c)\sin\theta$ transferred to the system can be adjusted by altering θ. At ν = 1/3, a reduction of θ from 25° to 10° results in a decrease of kl_B from ≈ 0.05 to an extremely small value ≈ 0.02, effectively approaching the long-wavelength limit ($q = k$ = 0). At ν = 1/3, the energy ratio of the spin-2 mode to Δ_m^R reaches 2.07 at $kl_B \approx 0.02$ (Fig. 3a and Extended Data Fig. 3) and decreases by 15% as kl_B increases to ≈ 0.05 (Figs. 1e and 2c), as guided in the red dashed line. At ν = 2/3, the energy ratio reaches 2.2 at $kl_B \approx 0.03$ with θ = 10° (Fig. 3b and Supplementary Fig. 3). The error bars originate from the uncertainty in determining the energy positions of these two modes in RILS spectra. Notably, at extremely small wavevectors, the measured energy ratios at ν = 1/3 and 2/3 are larger than the value (1.8 at zero wavevector) expected for a two-roton bound state (the black dashed arrow). The ratio for the two-roton bound state would increase with wavevectors but have to be lower than two because of its two-roton characteristic. We would like to mention that the large energy ratio at ν = 2/3 indicates that Δ_m^0 could be in the continuum of excitations. Interestingly, in CP-RILS measurements, Δ_m^0 is well resolved in the LL geometry, which indicates that the continuum does not have a large contribution in this geometry.

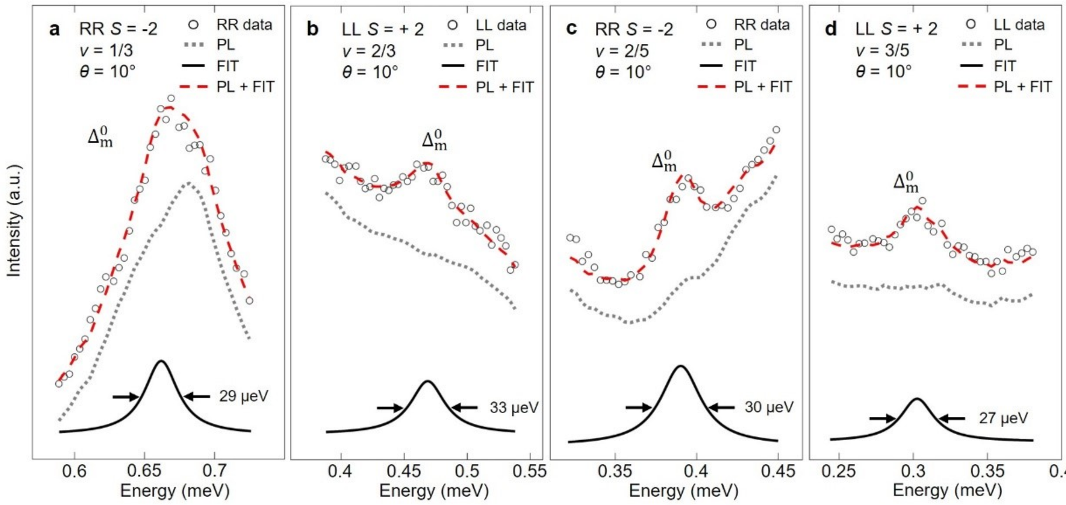

Extended Data Fig. 6. **Peak fitting of the Δ_m^0 modes at *v* = 1/3, *v* = 2/3, *v* = 2/5 and *v* = 3/5 with *θ* = 10°.** The black open dots represent the experimental signals of the Δ_m^0 modes in CP geometries (RR for *v* = 1/3 and *v* = 2/5, LL for *v* = 2/3 and *v* = 3/5). The grey dash lines indicate smoothed PL background signals. The black lines are the fitted Lorentzian peaks with small FWHM (29 μeV for *v* = 1/3, 33 μeV for *v* = 2/3, 30 μeV for *v* = 2/5 and 27 μeV for *v* = 3/5). The combination of these fitted Lorentzian peaks and PL background signals (the red dashed lines) gives a remarkable agreement to the measured RILS spectra. The sharpness of these peaks is noteworthy, as it indicates wavevector conservation in the scattering.

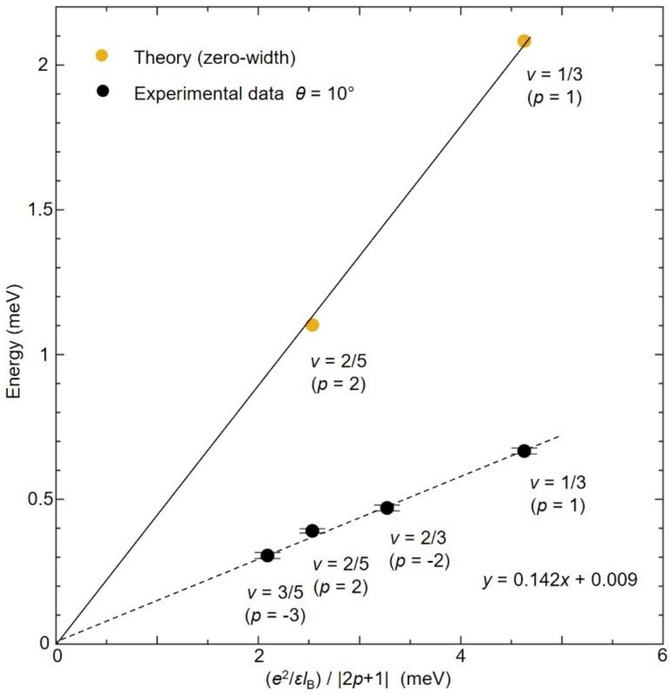

Extended Data Fig. 7. **Comparison of the measured Δ_{m}^{0} energies to theoretical calculations.** The yellow dots represent theoretical calculations of the Δ_{m}^{0} energies at $\nu = 1/3$ ($p = 1$) and $\nu = 2/5$ ($p = 2$), obtained from Ref. 29 for zero-width 2D systems. Theoretical values given in the reference in the unit of E_c are converted to meV scale using the density of our sample. The black dots represent experimental results obtained in our RILS measurements. These experimental results are taken at $\theta = 10°$ and correspond to filling factors $\nu = 1/3$ ($p = 1$), 2/3 ($p = -2$), 2/5 ($p = 2$) and 3/5 ($p = -3$). The error bars indicate the uncertainty in determining the energy positions in the RILS spectra. Both theoretical (yellow dots) and experimental (black dots) gap energies are found proportional to $(e^2/\varepsilon l_B)/|2p+1|$, characteristic of CFs moving under effective magnetic fields in the orbits, which determine the magnetoroton gaps. The dashed line represents an excellent linear fit of the experimental data, yielding a slope of 0.142 and y-intercept of 0.009 meV. The solid line is the guide to the eye.

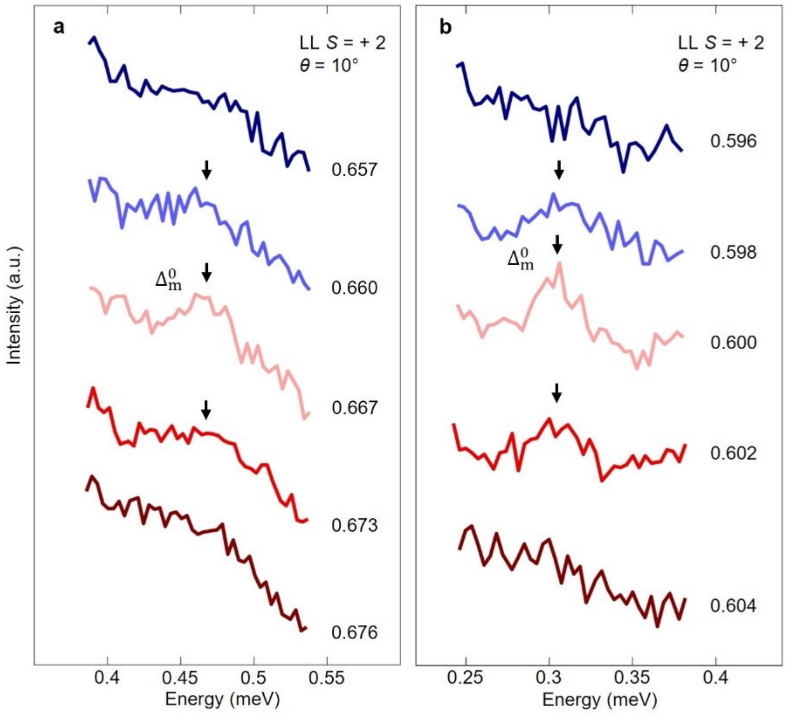

Extended Data Fig. 8. **Filling factor dependence of the Δ_m^0 modes at ν = 2/3 and 3/5 in the LL geometry with θ = 10°. a**, RILS spectra of the Δ_m^0 mode at filling factors around ν = 2/3. The mode intensity rapidly decreases as the filling factor deviates from ν = 2/3. **b**, RILS spectra of the Δ_m^0 mode at filling factors around ν = 3/5. A similar rapid decline in the mode intensity is observed as the filling factor moves away from ν = 3/5. The FQH effect is known for its incompressible behavior at specific fractional filling factors, and deviations from these filling factors make the system more compressible. The observed pronounced sensitivity to filling factors is characteristic of the FQH effect. RILS peaks are marked by vertical black arrows.

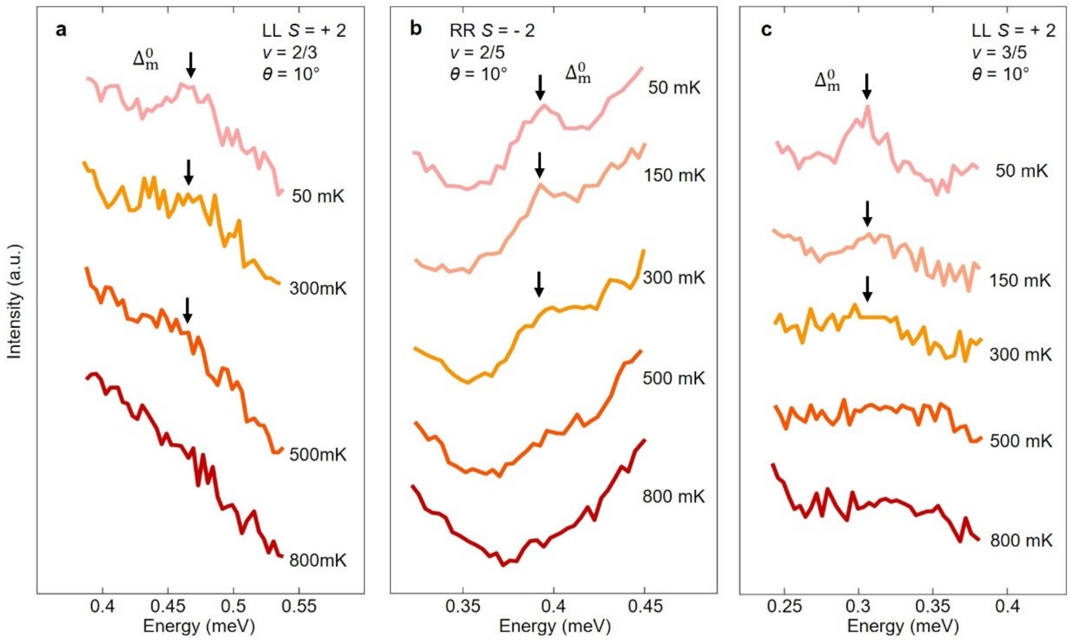

Extended Data Fig. 9. **Temperature dependence of the Δ_m^0 modes at FQH states with θ = 10°.** **a, b** and **c** present temperature dependence of the Δ_m^0 modes at ν = 2/3 (in the LL geometry), ν = 2/5 (in the RR geometry) and ν = 3/5 (in the LL geometry), respectively. As the temperature increases, the mode intensities are suppressed in all the three cases and the modes eventually vanish at 800 mK. In the FQH states, the formation of incompressible liquids results from strong electron-electron interactions with the presence of energy gaps. However, as the temperature rises, thermal excitations could disrupt the delicate correlated ground states, leading to the observed reduction in the mode intensity. RILS peaks are marked by vertical black arrows.

	Magnetoroton	Long wavelength	Spin-2	Chiral
Description	Determine 'masses' of the CGMs		Associated with the geometrical nature of the CGMs	Determined by the direction of B^* seen by the CFs
Experimental results	Linear energy scaling (Fig. 4c)	Sharp line-shape of the observed modes (Figs. 2f and 4b)	In prominent FQH states around half filling, each Δ_m^0 is dominated by one polarized component with total angular momentum of 2 (Figs. 2c and 3).	As shown in Fig. 4a, at $\nu = p/(2p+1)$, the modes carry S = -2 for electron states under positive B^* (for p > 0) and S = +2 for their particle-hole conjugates under negative B^* (for p < -1).
	Temperature and filling factor dependence (Figs. 2g, 4d, 4e, Supplementary Fig. 2, Extended Data Figs. 8 and 9)			
	Compare mode energies with magnetoroton dispersions to identify Δ_m^0 (Figs. 1e, Extended Data Fig. 3, Supplementary Figs. 3 and 5)			
	At ν = 1/3 and 2/3, energy ratios of such modes to Δ_m^R exclude the two-roton explanation and agree with the expectation for Δ_m^0.			

Extended Data Table 1. **Summary of the experimental results.** CGMs are characterized by their specific gaps ("masses"), spin-2 and chiral properties. In this table, we show that the experimental results capture these key elements.